Research article

Dia'aaldin J. Bisharat* and Daniel F. Sievenpiper*

Manipulating line waves in flat graphene for agile terahertz applications

https://doi.org/10.1515/nanoph-2017-0133
Received December 27, 2017; revised March 4, 2018; accepted March 21, 2018

Abstract: Reducing open waveguides enabled by surface waves, such as surface plasmon polaritons, to a one-dimensional line is attractive due to the potentially enhanced control over light confinement and transport. This was recently shown to be possible by simply interfacing two co-planar surfaces with complementary surface impedances, which support transverse-magnetic and transverse-electric modes, respectively. Attractively, the resultant "line wave" at the interface line features singular field enhancement and robust direction-dependent polarizations. Current implementations, however, are limited to microwave frequencies and have fixed functionality due to the lack of dynamic control. In this article, we examine the potential of using gate-tunable graphene sheets for supporting line waves in the terahertz regime and propose an adequate graphene-metasurface configuration for operation at room temperature and low voltage conditions. In addition, we show the occurrence of quasi-line wave under certain conditions of non-complementary boundaries and qualify the degradation in line wave confinement due to dissipation losses. Furthermore, we show the possibility to alter the orientation of the line wave's spin angular momentum on demand unlike conventional surface waves. Our results on active manipulation of electromagnetic line waves in graphene could be useful for various applications including reconfigurable integrated circuits, modulation, sensing and signal processes.

Keywords: graphene metasurface; one-dimensional wave; spin-momentum locking; surface impedance; terahertz photonics.

1 Introduction

The ability to focus and guide electromagnetic (EM) energy, such as light, is of great scientific interest and key to modern communications, sensing, and quantum processing technologies. In particular, extensive research has been done on localization and transmission of EM waves, known as surface waves (SWs), at the interface between two media due to their easily accessible, planar, and open boundary configuration [1]. For example, surface plasmon polaritons (SPP) [2] featuring subwavelength confinement may exist at air-metal interface, and Block SWs [3] featuring low attenuation loss may exist at the interface between air and periodic dielectric stacks. The properties of SWs can be tailored through interfacing different materials [4] or by altering the structure of the interface surface, for instance, via metasurfaces [5, 6]. Since these design approaches are scalable, they have been widely used for applications across the entire EM spectrum [7–9]. Notably, metasurfaces have paved the way for implementing transformation optics [10, 11]. However, once fabricated, the EM response of the structures is fixed, allowing only for limited functionality. By contrast, the prospect of dynamically altering the photonic properties of the constituent materials provides full active control over the overall desired device operation [12, 13].

Especially attractive is the use of graphene as a platform for active nanophotonic structures in the terahertz (THz) to mid-infrared regime [14, 15]. Excess of electrons or holes in this atomically thin material can produce collective plasmon oscillations with relatively long lifetime, hence lower dissipation losses than conventional metals [16, 17]. In addition, the doping level in graphene can be varied via electrostatic gating, hence allowing easy tuning of its photonic response [18, 19]. As a result, graphene properties have been exploited for numerous photonic applications [20–22], including the use of graphene metasurface as

***Corresponding authors: Dia'aaldin J. Bisharat,** Department of Electronic Engineering, City University of Hong Kong, Kowloon, Hong Kong SAR, China; and Electrical and Computer Engineering Department, University of California San Diego, La Jolla, California, 92093, USA, e-mail: dbisharat2-c@my.cityu.edu.hk. http://orcid.org/0000-0003-2229-2123; and **Daniel F. Sievenpiper,** Electrical and Computer Engineering Department, University of California San Diego, La Jolla, California, 92093, USA, e-mail: dsievenpiper@eng.ucsd.edu

a screen for modulating phase, polarization, steering, and absorption profiles of free-space beams [23–26]. However, for most functionalities involving in-plane routing of EM signals, the plasmonic modes must ideally be confined also laterally in the graphene sheet. This is known to occur in graphene nanoribbons, which support strongly localized edge modes besides the traditional surface modes [27–29]. Also recently, other one-dimensional (1D) guided modes in graphene were proposed by depositing a graphene layer onto a sculpted substrate with V-shaped wedge or groove channels [30–33]. However, these modes require specific geometries different from the usual flat sheet, and hence hinder the ability to route signals over reconfigurable arbitrary pathways over the graphene surface.

In this work, we propose a more versatile, agile graphene platform based on line waves (LW) [34]. This 1D EM mode forms as an interference product between transverse-magnetic (TM) and transverse-electric (TE) types of SWs, at the line interface between co-planar, complementary boundaries, which support the two decoupled modes, respectively. Given the open boundary nature of the structure, it decays away in both transverse directions from the infinitesimal line, where ideally a singular field concentration exists, hence the name "line wave". Meanwhile, the mode confinement (phase velocity) of LW is dependent on the parameters of the interfaced boundaries. In addition, due to the spatial symmetry-inversion of the boundaries about the propagation direction, the LW exhibits pseudospin-polarizations locked to the wavevector, making it immune to backscattering due to certain structural defects [35–37]. Here, we discuss the required conductivity profiles of a freestanding graphene sheet necessary for LW operation and present an adequate graphene-metasurface configuration. In addition, we examine the general characteristics of LW in case of non-complementary conditions and dissipation loss. Moreover, we analyze the spin angular momentum of LW and how that differs from other types of EM waves. Then, we illustrate some examples of the possible circuit functionalities using a tunable LW-based graphene platform. Our contribution to combining the unique properties of LW and graphene could advance emerging THz applications such as robust integrated photonics, strong light-matter interaction, quantum information processes, and reconfigurable systems.

2 Results and discussion

2.1 Principle analysis

To establish a criterion for the LW existence, we characterize the interfaced boundaries simply by isotropic surface impedances (Z_s). In general, using Z_s conditions, which relate the tangential electric (E) and magnetic (H) field components on the surface, allows for the analysis and control of SW modes on a certain surface boundary [38–41]. Distinctly, TM (TE) mode (also known as E (H) mode or p (s) polarization) may form on an inductive (capacitive) surface with positive (negative) sign of Z_s, specified as follows [42]:

$$Z_{TM} = \eta_0 \sqrt{1-n^2} = j\eta_0 / \zeta, \quad Z_{TE} = \eta_0 / \sqrt{1-n^2} = -j\eta_0 \times \zeta \qquad (1)$$

where η_0 (≈377Ω) is the intrinsic wave impedance in free space, n is the refractive index, and ζ is an arbitrary positive real number. When interfacing boundaries of Z_{TM} and

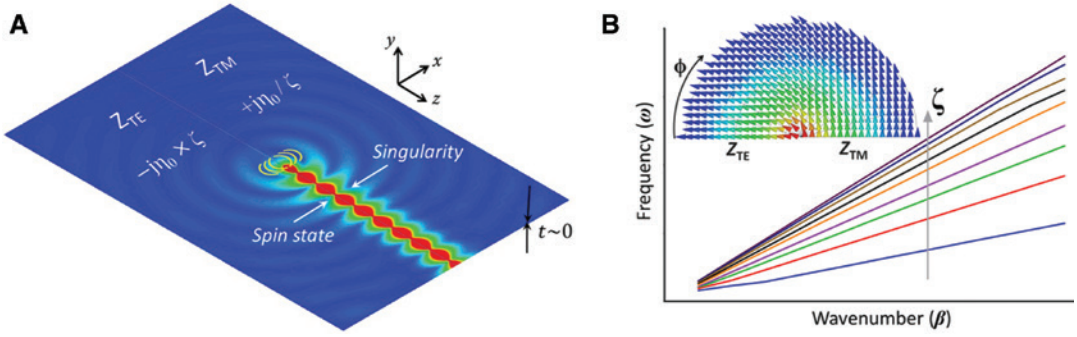

Figure 1: Formation and ideal characteristics of line wave.
(A) Magnitude distribution of the E-field across the interface between complementary TE and TM impedance surfaces showing the line wave formation with a direction-dependent polarization (pseudo-spin state) and maximum – ideally singular – field concentration along the interface line, and (B) the associated ideal dispersion relation at variable impedance values, hence confinement rates, as well as a vector plot of the E-field – in inset – showing the field's intensity decay in the radial direction away from the interface line, and the change in the field's vector orientation at different directions in the transverse plane to the interface line.

Z_{TE}, an effective cross coupling between the TM and TE modes occurs when there is no mismatch in wave momentum ($\beta = nk_0$, k_0 being the wavenumber in free space) across the interface. This corresponds to the two surfaces having identical ζ value, in which case they are considered complementary as they have equal but opposite effect on the E and H field components of the EM wave. As a result, the line interface preserves EM duality and a LW emerges, as shown in Figure 1, as desired.

Since doped graphene sheets may support both TM and TE plasmons [43–45], they may also be used to support LWs. The dispersion relations for TM and TE SWs along a freestanding graphene sheet in free space can be solved for β yielding [46]

$$\beta_{TM} = k_0\sqrt{1-(2/\sigma_g\eta_0)^2},\quad \beta_{TE} = k_0\sqrt{1-(\sigma_g\eta_0/2)^2} \tag{2}$$

where σ_g is the optical surface conductivity of graphene (see Section 4). Here, the factor of 2 takes into account the two-faced layout of the graphene sheet, i.e. $Z_{s(g)} = 2/\sigma_g$. Clearly, no SW propagation is possible for a real-valued σ_g, whereas for a pure-imaginary σ_g, a real solution with $\beta \geq k_0$ exists for TM (TE) mode at $\mathrm{Im}[\sigma_g] < 0$ ($\mathrm{Im}[\sigma_g] > 0$), as also directly inferred from Eq. (1). Figure 2A plots both real and imaginary parts of the actual σ_g as a function of frequency, with carrier relaxation lifetime $\tau = 0.5ps$. Here, $\mathrm{Re}[\sigma_g]$ spikes in a step-like fashion at $\omega\hbar = 2E_F$, where $\omega\hbar$ is the photon (plasmon) energy and E_F is the Fermi energy (i.e. chemical potential) of graphene. This is associated with the interband absorption of radiation, thus inhibiting SW formation [47]. In contrast, at zero temperature, both TM and TE exist without decay in the frequency ranges $\omega\hbar < 1.667E_F$ and $1.667E_F < \hbar\omega < 2E_F$, respectively. However, as temperature increases, $\mathrm{Re}[\sigma_g]$ becomes finite at all frequencies; hence, the modes acquire finite damping, and $\mathrm{Im}[\sigma_g]$ value within the TE range becomes limited.

As Figure 2B shows, the TM mode is generally tightly confined ($\mathrm{Re}[\beta] \gg k_0$) and is highly attenuated ($\mathrm{Im}[\beta] \gg k_0$) in the vicinity of the transition point, corresponding to $E_F = 0.15$ eV at frequency $\omega/2\pi = 60$ THz. In contrast, the TE mode extends significantly above the surface as its dispersion relation closely follows the free-space wave and is lightly damped. Due to the discrepancy between the confinement factors of the two modes, it is not plausible to use a freestanding graphene sheet to support LW operation at room temperature. The mismatch in wavenumbers may be alleviated by adding a dielectric cladding to the graphene layer hosting the TE mode in order to increase the associated mode confinement. In such case, it is necessary, however, to evaluate the effect of the possible difference in dielectric constant between a substrate and superstrate on the TE mode formation. Assuming a vacuum superstrate and a dielectric substrate are used, we find that the TE mode exists only when $\varepsilon_r - 1 < (4\alpha\mathrm{Im}[\sigma_g]/\sigma_0)^2$, where ε_r is the dielectric constant, $\alpha \approx 1/137$ is the fine-structure constant, and $\sigma_0 = e^2/\pi\hbar$ is the characteristic conductivity [48]. Evidently, the allowable deviation ($<10^{-3}$ for $\hbar\omega < 2E_F$) in dielectric values is trivial, thus practically excluding the potential use of any substrate.

2.2 Proposed structure

Alternatively, we propose the use of a graphene-metasurface configuration such as shown in the schematic in Figure 3A. The parallel stack structure is made of a layer consisting of periodic subwavelength arrangement of

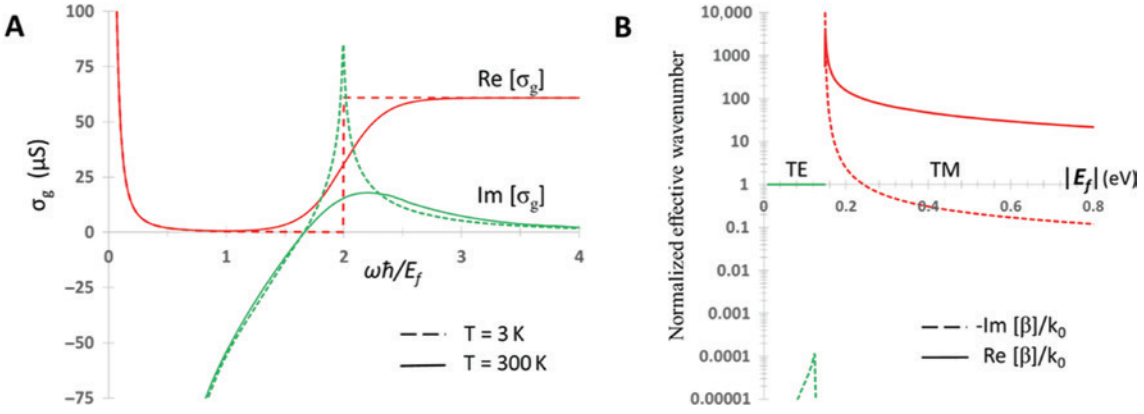

Figure 2: Surface conductivity of graphene and associated surface waves.
(A) Surface conductivity of graphene as a function of frequency (normalized by chemical potential) at different temperatures (T), and (B) surface wave propagation constant (normalized by free-space wavenumber) as a function of chemical potential at $\omega_\hbar = 0.26$ eV ($\omega/2\pi = 60$ THz).

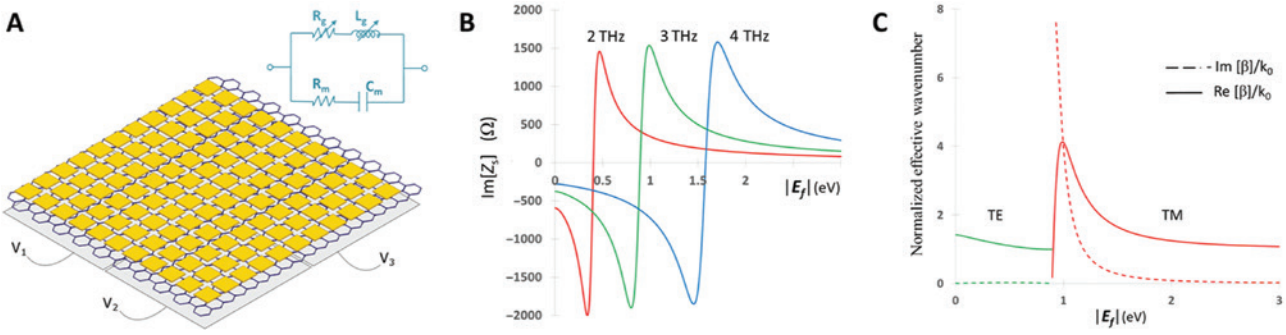

Figure 3: Details of the proposed structure and associated properties.
(A) Schematic of the proposed LW platform based on graphene-metasurface and the corresponding circuit model of a parallel transmission line in the inset, (B) the surface reactance of the structure as a function of chemical potential at different frequencies, and (C) the associated SW propagation constants as a function of chemical potential at $\omega/2\pi = 3$ THz.

metallic patches, which has an effective capacitive EM response, and a graphene layer, which has an inductive EM response. Here, it becomes possible to make better use of the graphene properties by operating in the low THz regime, where graphene's conductivity (hence, $Z_{s(g)}$) can be significantly tuned and dissipation losses are minimum [49]. For in-plane wave propagation, the structure response can be modeled as parallel transmission lines (i.e. $1/Z_s = 1/Z_{s(g)} + 1/Z_{s(m)}$), where the surface impedance of the metasurface, assuming it has zero resistance, is [50, 51]

$$Z_{s(m)} = \frac{-j\eta_0}{2a\frac{k_0}{\pi}\ln\left[\csc\left(\frac{\pi g}{2a}\right)\right]} / \varepsilon_{eff} \tag{3}$$

where $a = 10$ μm is the unit cell size, $g = 1$ μm is the gap spacing between adjacent patches, and $\varepsilon_{\text{eff}} = 1.4$ is the effective dielectric constant. Note that since depositing metal directly on a graphene sheet changes its conductivity significantly, here we consider an isolation layer of SiO_2 with a thickness of 0.2 μm (see Section 4). Accordingly, by altering the impedance of the graphene sheet, while that of the metasurface layer remains fixed at a given frequency, the effective net response of the overall structure can be varied from capacitive to inductive, as shown in Figure 3B. In the meanwhile, at any given chemical potential the structure's EM response switches from inductive at the lower frequency end to capacitive towards higher frequencies.

As Figure 3C shows, at low values of E_F, TE mode is supported with relatively greater confinement than that of the previously studied case of isolated graphene sheet. Specifically, for the given structure parameters, the confinement factor at 3THz spans $1 < \text{Re}[\beta_{TE}]/k_0 < 1.42$ and decreases with the increase of E_F, as expected. As E_F is increased further, a TM mode appears instead with a maximum confinement close to the transition point. For the range $0.9 < E_F < 3$, a confinement factor of $1 < \text{Re}[\beta_{TM}/k_0] < 4.1$ is obtained. Since similar momenta of the two modes are attainable in the range $1 < \text{Re}[\beta/k_0] < 1.42$ with little attenuation ($\text{Im}[\beta]/k_0 < 0.2$), the proposed structure proves capable of supporting LW at room temperature. The possible LW's operation range is determined by the practical limitations incurred by both modes. Particularly, the TE momentum has an upper limit that is set by the fixed capacitive response of the metasurface, whereas the TM momentum has a lower limit that is set by the highest achievable inductive response of the graphene sheet (i.e. E_F). Note that while the upper limit incurred by TE mode can be improved by increasing the capacitance of the metasurface, for instance, by shrinking its gaps, this necessitates a higher chemical potential of graphene to maintain the lower limit incurred by the TM mode, and vice versa.

In general, since the energy dispersion (i.e. electronic density of states) in graphene is linear and gapless around its charge neutrality (Dirac) point, σ_g can be varied significantly with carrier concentration (N) compared to other materials, as $E_F = \hbar v_F \sqrt{\pi N}$, where v_F ($\approx 10^8$ cm s^{-1}) is the Fermi velocity [52]. However, as its energy states are filled, it becomes predictably harder to raise E_F. Here, N can be increased via chemical doping or by applying electrostatic bias to the graphene sheet, as illustrated in Figure 3A, via gate voltage. The first approach, which entails adding dopant atoms to graphene, would increase the carrier scattering rate, τ^{-1}, thus increasing the dissipation loss, whereas in the latter approach, an applied voltage exceeding the breakdown threshold of the supporting dielectric layer would render the devise obsolete. In contrast,

the use of top-gated ionic gel has been experimentally shown to be capable of providing doping levels up to $N = 1.0 \times 10^{14}\text{cm}^{-2}$, hence $E_F \approx 1.6\text{eV}$, with a low gate voltage $V_g \approx 4$ V [53, 54]. This is as a result of its high gate capacitance ($C_{\text{EDL}} \approx 2\mu\text{F cm}^{-2}$) due to the formation of a thin electric double layer (thickness ≈1 nm) close to the graphene surface. Acting as one of the formed capacitor plates, the graphene sheet would thus have a charge carrier concentration of $N = C_{\text{EDL}} V_g / e$.

Here, we propose the use of ion-based solid electrolyte, which exhibits similar performance to ion-gel designs but can be used as both a back gate and a substrate to support graphene, hence allowing easier implementation and more device functionalities [55, 56]. In addition, we propose the use of multilayer graphene sheets in order to achieve higher Fermi energy, given a fixed bias voltage. Being electrically connected and having negligible separation, the injected carriers due to a bias voltage are distributed among the different graphene layers [57]. As the extra carriers add up to the total charge in the gate capacitor, the equivalent Femi level corresponds to the sum of the individual levels, leading to an increase in total conductivity proportionally to the number of layers (n), as follows [58]:

$$\sigma_g^{\text{total}} = \sigma_g^1 + \ldots + \sigma_g^n = \frac{-je^2 \sum_{i=1}^{n} |E_F^{(i)}|}{\pi \hbar^2 (\omega - j\tau^{-1})} \tag{4}$$

The above Drude conductivity model is valid since the intraband contribution is dominant at the operating range under consideration. Furthermore, note that the carrier scattering rate and mobility in multilayer graphene remain conveniently similar to that in a single layer [58]. Therefore, a good performance is attainable using only three layers of graphene, where $E_F = 3$ eV merely requires $V_g = 1.56$ V.

2.3 Line mode characteristics

Figure 4A shows the propagation characteristics at 3THz of the LW with different ζ values, at which the complementary surfaces have the relation $\text{Im}[Z_{TM}] \times \text{Im}[Z_{TE}] = \eta_0^2$. The attainable modes, with $1.05 < \zeta < 2.47$, have a normalized propagation constant of $1.6 < \text{Re}[\beta/k_0] < 5.9$ with the maximum occurring at $\zeta = 1.13$. On the other hand, the figure-of-merit $\text{Re}[\beta]/\text{Im}[\beta]$ dictating the relative propagation length of the mode increases proportionally with the increase of ζ due to diminishing attenuation. Figure 4B plots the propagation results at $\zeta = 1.94$ as a function of distance between the interfaced regions, over which a linear rather than abrupt transition (see inset) is assumed in the conductivity profile of the graphene sheet. While the propagation length decreases with larger transition distances (d), as expected, the LW characteristics are roughly unchanged at $d \leq 1$ μm. Therefore, the proposed configuration proves adequate for supporting operational LW modes within the limited range of Z_s values of the proposed structure under realistic conditions.

To probe the LW properties more systematically, Figure 4C shows the effect of dissipation loss on the confinement and propagation factors of LW as a function ζ. Here, we use the actual complex conductivities of graphene on both TE and TM sides of the LW and multiply the real part of the overall surface impedance by a factor of $0 \leq \delta \leq 1$, where 0 corresponds to the lossless case. While the LW tends to maximum confinement at the lower limit $\zeta = 1$, the effective propagation length increases proportionally with ζ, indicating a trade of between the two factors. In addition, the LW confinement is deteriorated due to loss, predominantly at lower ζ values, indicating a dependence of the LW propagation constant on $\text{Re}[Z_s]$ rather than solely on $\text{Im}[Z_s]$. Meanwhile, Figure 4D compares the normalized intensity profile of E-field distribution of the LW in the transverse direction across the line interface at different ζ values. Favorably, the LW features a comparable, albeit slightly less lateral energy concentration at higher ζ values, making such values equally fit for 1D waveguide operation. Moreover, the associated moderate mode confinement makes it easy to couple external waves, for instance in air, to the LWs due to the little momentum mismatch.

We note that an interface between inductive and capacitive impedance surfaces of non-complimentary values can support a quasi-line mode. As shown in Figure 5A, this mode exhibits similar field profiles to traditional edge modes, indicating that LW and edge mode share similar characteristics [59]. An implementation of the quasi-line mode has been recently studied based on a graphene/graphene platform at low temperature [60]. Figure 5B plots the normalized propagation constants of the quasi-line modes in the lossless case along with that of the conventional 2D SW. These 1D modes show two notable properties: they exhibit sharp increase in confinement reciprocally with ζ, at either side of the interface; and they cease to exist when $Z_{TM} > -Z_{TE}$. The later property is in agreement with the observation that no LW is supported at $\zeta < 1$, while the former property is akin to the asymptotic behavior of LW (see Figure 4C) presumably towards infinite confinement (i.e. zero wave speed) at $\zeta = 1$. For the

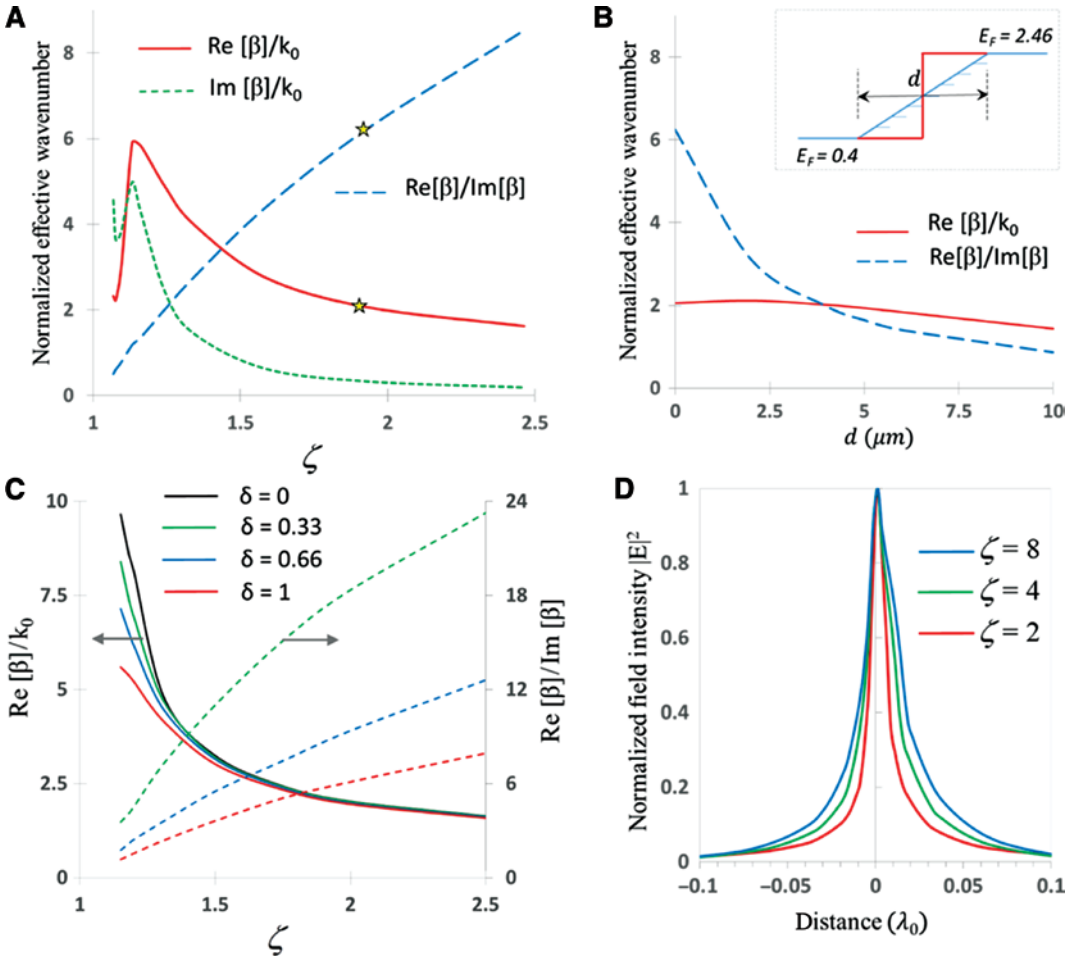

Figure 4: Numerical simulation of the line wave's mode properties under different conditions.
(A) Propagation characteristics of LWs with different ζ values supported by the graphene metasurface at 3 THz, (B) associated propagation characteristic of the structure at $\zeta = 1.94$ in the case of non-abrupt, linear change in Femi energy of graphene – as illustrated in the inset – over different distances across the line interface, (C) general relation of confinement and propagation factors of LWs versus ζ with prescribed values of loss factor ($\mathrm{Re}[Z_s]_{new} = \delta\ \mathrm{Re}[Z_s]_{actual}$), and (D) general field intensity profile distribution in the transverse direction to the line interface, over the surface, for LWs of different ζ values.

sake of clarity, unsteady results from our full-wave simulations near $Z_{TM} = -Z_{TE}$ and $\zeta = 1$ have been excluded from the presented figures. Nonetheless, the asymptotic limit of the wavenumbers for LW and quasi-line mode is evident from the increase in mode confinement, which diverges relative to that of SW [2] on similar Z_s surface towards lower ζ values.

2.4 Optical spin-orbit interaction

Recently, it has been shown that evanescent waves universally possess spin angular momentum tied to the propagation direction [61]. This coupling occurs in TM (TE) SWs due to the wave confinement in the perpendicular direction to propagation axis, leading to a longitudinal component of the E (H) field with a $\pm\pi/2$ phase difference relative to the field component normal to the surface [62]. As such, the E (H) field vector rotates in the plane normal to the surface (i.e. is elliptically polarized) resulting in a purely transverse spin component that flips sign with the reversal of propagation direction. In contrast, circularly polarized (CP) plane waves in free space have purely longitudinal spin that is in the range [–1, 1] (i.e. parallel or anti-parallel to the wavevector) depending on the helicity of the mode. The decay of EM fields in the two directions orthogonal to propagation axis in the case of LW, which leads to the presence of all six EM field components, makes LW different from the aforementioned cases. This mode is essentially a hybrid of TE and TM modes yet exhibits a different spin orientation from that of either mode.

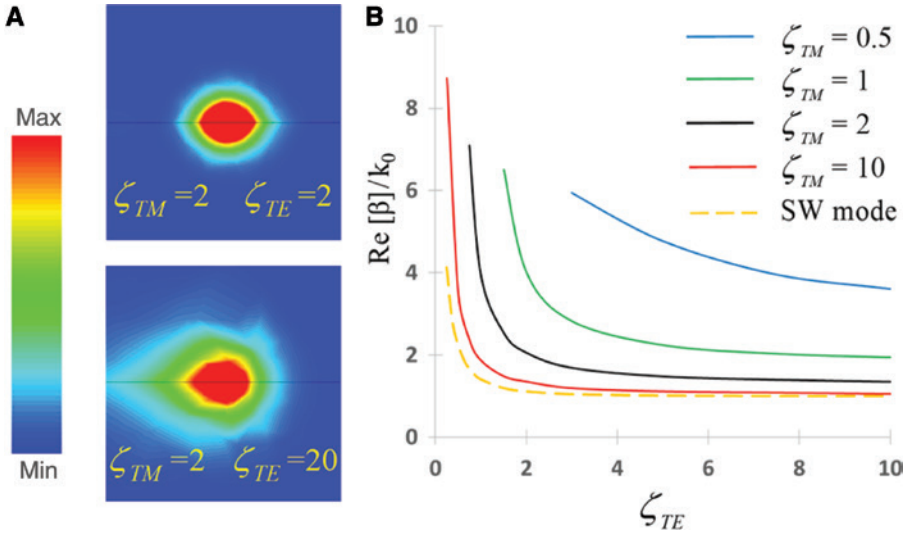

Figure 5: Numerical simulation of the quasi-line mode confinement properties.
(A) Distribution of the E-field magnitude over a cross-sectional area within the transverse plane to the propagation direction of the line mode (top) and a quasi-line mode (bottom), and (B) normalized propagation constant (confinement factor) of the quasi-line mode at different surface impedance values in case of non-complementary and lossless impedance surfaces across the line interface and comparison with conventional surface wave (SW) mode.

The spin orientation can be understood from Figure 6A, which depicts the rotation of both E and H field vectors at an angle with respect to the surface. The value of the local spin density (in units of $\hbar$ per photon) is determined by the relation [63]

$$\mathbf{S} = \frac{\mathrm{Im}[\mathbf{E}^* \times \mathbf{E} + \mathbf{H}^* \times \mathbf{H}]}{W} \tag{5}$$

where $W = |\mathbf{E}|^2 + |\mathbf{H}|^2$ is the local energy density of the fields. Figure 6B plots the spin magnitude and the relative contribution of the individual spin components (e.g. $S'_x = \mathbf{S} \cdot \hat{x}/|\mathbf{S}|$) in the vicinity of the line interface above the surface. Clearly, the orientation angle of the spin in the transverse *xy* plane is variable depending on the relative Z_s values across the line interface. In addition, a longitudinal spin emerges upon the introduction of loss to the supporting surface. As such, unlike conventional SWs, the spin orientation relative to the propagation direction of LW could be flexibly tuned. This observation also applies to the case of quasi-line modes, making such tunability easily attainable.

The spin-momentum locking property allows for robust unidirectional flow of evanescent waves in general via an excitation beam carrying similar spin angular

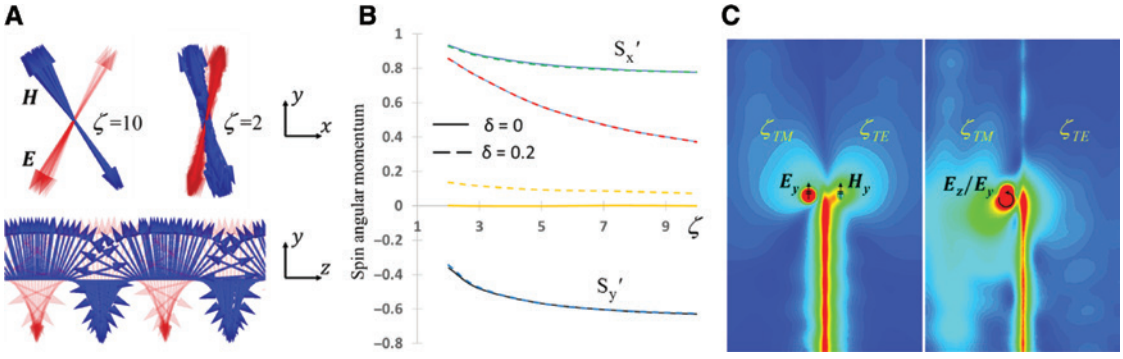

Figure 6: Spin angular momentum properties of line wave.
(A) Snapshot in time of electric and magnetic field vectors of LW along the propagation axes with a cross-section view (top) and longitudinal section view (bottom), (B) magnitude of spin angular momentum (red) and normalized contributions of the spin components along different directions of the LW as a function of ζ with and without loss, and (C) E-field magnitude distribution over the surface showing directional excitation of LW via a CP electric dipole (left) and a pair of linearly polarized, in-phase electric and magnetic dipoles (right) on opposite sides of the line interface.

momentum [64]. This is usually tested through the near field of a point source CP electric dipole placed in the vicinity of a TM-supportive surface [65]. Likewise, a CP magnetic dipole may excite a directional SW mode over a TE-supportive surface. The LW may be excited with either source since its spin relies on the dual contribution of the E and H fields as shown in Eq. (5). As shown in Figure 6C, it can also be excited using a dipole pair of different types that are placed within half-wavelength distance apart across the line interface. Here, the linearly polarized parallel dipoles excite SWs respectively omni-directionally, proving that the unidirectional excitation of the LW is not simply due to that of the surrounding SWs. Instead, it is due to the phase relation between E and H fields, given that the two components have a phase combination that is unique to a particular spin orientation. This property along with the tunability of the spin orientation of LW offers a new degree of freedom for manipulating wave-matter interactions, such as routing the flow of photoluminescence depending on the polarization of the emitter transition [66], which has attracted focused interest lately for use in quantum signal processes.

2.5 Reconfigurable circuits

Many recent research works have been done on transmission line structures with high field concentration [67–69] including based on spoof SPP at the THz regime [70, 71]. However, the majority of the associated applications lack reconfigurability, enabling only limited circuit functionality. Figure 7A shows a schematic of an agile, versatile platform based on graphene-LW combination. By using a large array of bias control pads beneath the structure, we could guide signals along arbitrary pathways between selectively different inputs/outputs. Since the orientation of the impedance surfaces across the line interface is reversed in the backward/forward propagation directions, the associated spin orientations are opposite, allowing the corresponding orthogonal polarization states of LW to be used for transmitting and receiving of signals without interference. In addition, the associated robustness could be exploited to alter the surface impedances across the line interface to control the mode confinement at specific sections along the waveguide for use as compact delay lines with tunable phase shift [34]. Moreover, since switching the impedance surface type across the interface at a particular section would forbid further propagation of a given LW polarization, this can be used as a switching functionality or for implementing network devices such as the magic-T structure shown in Figure 7C.

3 Conclusion

In summary, we have discussed the properties of LWs and proposed a practical implementation in flat graphene, which allows for their dynamic manipulation. Specifically, a stack of multilayer graphene and a metallic patch metasurface over a back-gated electrolyte substrate was shown to emulate the necessary impedance surfaces using low bias voltage variation at room temperature. Unlike other 1D modes, our approach based on LWs allows for readily reconfigurable wave pathways, mode confinement, and polarization states. In addition, LWs are attractive for sensing and potentially nonlinear applications due to the higher mode confinement compared to conventional SWs. Furthermore, we have shown that LWs exhibit unique flexible optical spin-momentum relation, which could

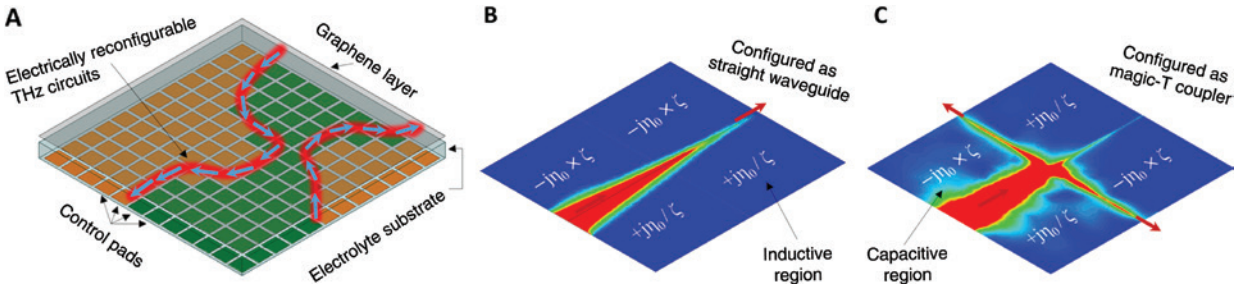

Figure 7: Illustration of an electrically programmable platform of line waves for (A) guiding signals along arbitrary-shaped pathways, (B) robust straight delay lines with tunable phase shift capability, and (C) network circuits such as a magic-T coupler based on spin-filtered channels.

The arrows indicate one sense of polarization that is specific to the shown propagation direction due to spin-momentum locking. Figures B and C show the full-wave simulation results of the electric field intensity distribution above the surface of the proposed graphene metasurface structure with the actual complex conductivities corresponding to $\zeta = 2.4$.

be beneficial for circuits based on spintronic processes. Moreover, we have pointed out the occurrence of quasi-LWs under certain conditions of non-complementary boundaries, which exhibit similar characteristics to LW albeit with asymmetric field profile and lower field concentration. Finally, although our study concerns graphene at the low THz regime, our results may be extended to similar 2D materials at other frequencies [49, 72, 73], allowing for potentially more applications and improved performance.

4 Methods

4.1 Graphene conductivity

In our classical approach, the EM response of the graphene sheet is derived from its optical surface conductivity (σ_g). In the absence of external magnetic field, this is given in the local limit of the random-phase approximation at a finite temperature by [15, 17]

$$\sigma_g(\omega, E_F, \tau, T) = \sigma^{\text{intra}}(\omega, E_F, \tau, T) + \sigma^{\text{inter}}(\omega, E_F, \tau, T)$$

$$\sigma^{\text{intra}} = \frac{-je^2}{\pi\hbar^2(\omega - j\tau^{-1})}\left\{E_F + 2k_BT\ln\left[\exp\left(\frac{-E_F}{k_BT}\right)+1\right]\right\}$$

$$\sigma^{\text{inter}} = \frac{e^2}{4\hbar}\left(\frac{1}{2} + \frac{1}{\pi}\arctan\left[\frac{\omega\hbar - 2E_F}{2k_BT}\right] + \frac{j}{2\pi}\ln\left[\frac{(\omega\hbar + 2E_F)^2}{(\omega\hbar - 2E_F)^2 + (2k_BT)^2}\right]\right) \quad (6)$$

where ω is the angular frequency, e is the electron charge, k_B is the Boltzmann constant, T is the temperature, $\hbar$ is the reduced Planck constant, τ is the carrier relaxation lifetime, and E_F is the Fermi energy. The first (second) term is attributed to intraband (interband) transition (i.e. electron-photon scattering process), which is dominant for $\omega\hbar \ll 2E_F$ ($\omega\hbar \geq 2E_F$), in which case the sheet's response is inductive (capacitive).

In our study, where high doping at room temperature and frequencies are well below $2E_F$, we can safely neglect temperature and interband effects, which reduces the expression above for σ_g to the Drude conductivity model given in Eq. (4).

4.2 Numeral analysis

Full-wave simulations were performed using the Eigenmode setup (for dispersion relations) and Driven-mode setup (for transmission data) in ANSYS HFSS, which is a finite element method-based commercial software. The graphene was modeled as a sheet of zero thickness with an assigned isotropic impedance value (i.e. surface impedance boundary). The metallic patch metasurface was modeled as perfect electric conductor of finite size. Unit cell incorporating the stacked two layers with an isolation dielectric was solved for using periodic boundaries, and the extracted effective net impedance was found to be in agreement with the theoretical calculations of the parallel transmission line model in Figure 3B. Here, $\varepsilon_{\text{eff}} = (t\varepsilon_r + 1)/2$, where $(1/\varepsilon_r) < t < 1$ is a constant dependent on the dielectric layer thickness. Subsequently, the overall structure was modeled as two adjacent semi-infinite surface impedance boundaries, with values corresponding to Z_{TM} and Z_{TE} across the interface of LW.

Acknowledgments: This work has been supported in part by AFOSR grant FA9550-16-1-0093.

References

[1] Polo JA Jr., Lakhtakia A. Surface electromagnetic waves: a review. Laser Photon Rev 2011;5:234–46.
[2] Maier SA. Plasmonics: fundamentals and applications. New York, USA, Springer-Verlag, 2007.
[3] Meade RD, Brommer KD, Rappe AM, Joannopoulos JD. Electromagnetic Bloch waves at the surface of a photonic crystal. Phys Rev B 1991;44:10961–4.
[4] Ramos-Mendieta F, Halevi P. Electromagnetic surface modes of a dielectric superlattice: the supercell method. J Opt Soc Am B 1997;14:370–81.
[5] Holloway CL, Kuester EF, Gordon JA, O'Hara J, Booth J, Smith DR. An overview of the theory and applications of metasurfaces: the two-dimensional equivalents of metamaterials. IEEE Antennas Propag Mag 2012;54:10–35.
[6] Garcia-Vidal FJ, Martín-Moreno L, Pendry JB. Surfaces with holes in them: new plasmonic metamaterials. J Opt A: Pure Appl Opt 2005;7:S97–101.
[7] Kildishev AV, Boltasseva A, Shalaev VM. Planar photonics with metasurfaces. Science 2013;339:1232009.
[8] Williams CR, Andrews SR, Maier SA, Fernández-Domínguez AI, Martín-Moreno L, García-Vidal FJ. Highly confined guiding of terahertz surface plasmon polaritons on structured metal surfaces. Nat Photon 2008;2:175–9.
[9] Yu L, Barakat E, Sfez T, Hvozdara L, Francesco JD, Herzig HP. Manipulating Bloch surface waves in 2D: a platform concept-based flat lens. Light Sci Appl 2014;3:e124.
[10] Werner DH, Kwon DH. Transformation electromagnetics and metamaterials. London, UK, Springer-Verlag, 2014.
[11] Xu L, Chen H. Conformal transformation optics. Nat Photon 2015;9:15–23.
[12] Shaltout AM, Kildishev AV, Shalaev VM. Evolution of photonic metasurfaces: from static to dynamic. J Opt Soc Am B 2016;33:501–10.

[13] Zheludev NI, Kivshar YS. From metamaterials to metadevices. Nat Mater 2012;11:917–24.
[14] Tassin P, Koschny T, Soukoulis CM. Graphene for terahertz applications. Science 2013;341:620–1.
[15] Low T, Avouris P. Graphene plasmonics for terahertz to mid-infrared applications. ACS Nano 2014;8:1086–101.
[16] He X, Gao P, Shi W. A further comparison of graphene and thin metal layers for plasmonics. Nanoscale 2016;8:10388–97.
[17] Xiao S, Zhu X, Li B-H, Mortensen NA. Graphene-plasmon polaritons: from fundamental properties to potential applications. Front Phys 2016;11:117801.
[18] Gao W, Shi G, Jin Z, et al. Excitation and active control of propagating surface plasmon polaritons in graphene. Nano Lett 2013;13:3698–702.
[19] He X, Lin F, Liu F, Shi W. Terahertz tunable graphene Fano resonance. Nanotechnology 2016;27:485202.
[20] Bao Q, Loh KP. Graphene photonics, plasmonics, and broadband optoelectronic devices. ACS Nano 2012;6:3677–94.
[21] Wong LJ, Kaminer I, Ilic O, Joannopoulos JD, Soljačić M. Towards graphene plasmon-based free-electron infrared to X-ray sources. Nat Photon 2016;10:46–52.
[22] Rodrigo D, Limaj O, Janner D, et al. Mid-infrared plasmonic biosensing with graphene. Science 2015;349:165–8.
[23] Yao Y, Shankar R, Kats MA, et al. Electrically tunable metasurface perfect absorbers for ultrathin mid-infrared optical modulators. Nano Lett 2014;14:6526–32.
[24] He X. Tunable terahertz graphene metamaterials. Carbon 2015;82:229–37.
[25] Sherrott MC, Hon PWC, Fountaine KT, et al. Experimental demonstration of >230° phase modulation in gate-tunable graphene – gold reconfigurable mid-infrared metasurfaces. Nano Lett 2017;17:3027–34.
[26] Dutta-Gupta S, Dabidian N, Kholmanov I, Belkin MA, Shvets G. Electrical tuning of the polarization state of light using graphene-integrated anisotropic metasurfaces. Phil Trans R Soc A 2017;375:20160061.
[27] Nikitin AY, Guinea F, Garcia-Vidal FJ, Martín-Moreno L. Edge and waveguide terahertz surface plasmonmodes in graphene microribbons. Phys Rev B 2011;84:161407.
[28] Christensen J, Manjavacas A, Thongrattanasiri S, Koppens FHL, García de Abajo FJ. Graphene plasmon waveguiding and hybridization in individual and paired nanoribbons. ACS Nano 2012;6:431–40.
[29] Fei Z, Goldflam MD, Wu J-S, et al. Edge and surface plasmons in graphene nanoribbons. Nano Lett 2015;15:8271–6.
[30] Liu P, Zhang X, Ma Z, Cai W, Wang L, Xu J. Surface plasmon modes in graphene wedge and groove waveguides. Opt Express 2013;21:32432–40.
[31] Cui J, Sun Y, Wang L, Ma P. Graphene plasmonic waveguide based on a high-index dielectric wedge for compact photonic integration. Optik 2016;127:152–5.
[32] Gonçalves PAD, Dias EJC, Xiao S, Vasilevskiy MI, Mortensen NA, Peres NMR. Graphene plasmons in triangular wedges and grooves. ACS Photonics 2016;3:2176–83.
[33] Ansell D, Radko IP, Han Z, Rodriguez FJ, Bozhevolnyi SI, Grigorenko AN. Hybrid graphene plasmonic waveguide modulators. Nat Commun 2015;6:8846.
[34] Bisharat DJ, Sievenpiper DF. Guiding waves along an infinitesimal line between impedance surfaces. Phys Rev Lett 2017;119:106802.
[35] Chen W-J, Zhang ZQ, Dong J-W, Chan CT. Symmetry-protected transport in a pseudospin-polarized waveguide. Nat Commun 2015;6:8183.
[36] Xu X, Li Y, Miao X. Robust waveguide against surface perturbations due to band inversion in two kinds of single-negative metamaterials. EPL 2016;116:44001.
[37] Slobozhanyuk A, Mousavi SH, Ni X, Smirnova D, Kivshar YS, Khanikaev AB. Three-dimensional all-dielectric photonic topological insulator. Nat Photon 2017;11:130–6.
[38] Gok G, Grbic A. Tailoring the phase and power flow of electromagnetic fields. Phys Rev Lett 2013;111:233904.
[39] Quarfoth R, Sievenpiper D. Artificial tensor impedance surface waveguides. IEEE Trans Antennas Propag 2013;61:3597–606.
[40] Patel AM, Grbic A. Transformation electromagnetics devices based on printed-circuit tensor impedance surfaces. IEEE Trans Microw Theory Techn 2014;62:1102–11.
[41] Lee J, Sievenpiper DF. Patterning technique for generating arbitrary anisotropic impedance surfaces. IEEE Trans Antennas Propag. 2016;64:4725–32.
[42] Sievenpiper D, Zhang L, Broas RFJ, Alexopolous NG, Yablonovitch E. High-impedance electromagnetic surfaces with a forbidden frequency band. IEEE Trans Microw Theory Techn 1999;47:2059–74.
[43] Mikhailov SA, Ziegler K. New electromagnetic mode in graphene. Phys Rev Lett 2007;99:016803.
[44] Vakil A, Engheta N. Transformation optics using graphene. Science 2011;332:1291–4.
[45] He XY, Tao J, Meng B. Analysis of graphene TE surface plasmons in the terahertz regime. Nanotechnology 2013;24:345203.
[46] Hanson GW. Dyadic Green's functions and guided surface waves for a surface conductivity model of graphene. J App Phys 2008;103:064302.
[47] Jablan M, Buljan H, Soljačić M. Plasmonics in graphene at infrared frequencies. Phys Rev B 2009;80:245435.
[48] Christensen T. Classical graphene plasmonics. In: Christensen T., ed. Classical to quantum plasmonics in three and two dimensions. Cham, Switzerland, Springer Theses Series; Springer, 2017, 97–129.
[49] Chen P-Y, Argyropoulos C, Farhat M, Gomez-Diaz JS. Flatland plasmonics and nanophotonics based on graphene and beyond. Nanophotonics 2017;6:1239–62.
[50] Luukkonen O, Simovski C, Granet G, et al. Simple and accurate analytical model of planar grids and high-impedance surfaces comprising metal strips or patches, IEEE Trans Antennas Propag 2008;56:1624–32.
[51] Padooru YR, Yakovlev AB, Kaipa CSR, Hanson GW, Medina F, Mesa F. Dual capacitive-inductive nature of periodic graphene patches: transmission characteristics at low-terahertz frequencies. Phys Rev B 2013;87:115401.
[52] Novoselov KS, Geim AK, Morozov SV, et al. Two-dimensional gas of massless Dirac fermions in graphene. Nature 2005;438:197–200.
[53] Aygar AM, Balci O, Cakmakyapan S, Kocabas C, Caglayan H, Ozbay E. Comparison of back and top gating schemes with tunable graphene fractal metasurfaces. ACS Photonics 2016;3:2303–7.
[54] Hu H, Zhai F, Hu D, et al. Broadly tunable graphene plasmons using an ion-gel top gate with low control voltage. Nanoscale 2015;7:19493–500.

[55] Zhao J, Wang M, Li H, et al. Lithium-ion-based solid electrolyte tuning of the carrier density in graphene. Sci Rep 2016;6:34816.
[56] Kakenov N, Balci O, Takan T, Ozkan VA, Altan H, Kocabas C. Observation of gate-tunable coherent perfect absorption of terahertz radiation in graphene. ACS Photonics 2016;3:1531–5.
[57] Yan X, Li X, Chandra B, et al. Tunable infrared plasmonic devices using graphene/insulator stacks. Nat Nanotechnol 2012;7:330–4.
[58] Rodrigo D, Tittl A, Limaj O, García de Abajo FJ, Pruneri V, Altug H. Double-layer graphene for enhanced tunable infrared plasmonics. Light Sci Appl 2017;6:e16277.
[59] Chamanara N, Caloz C. Fundamentals of graphene magnetoplasmons: principles, structures and devices. Forum Electromag Res Methods Appl Tech (FERMAT) 2015;10:1–15.
[60] Forati E, Hanson GW. Surface plasmon polaritons on soft-boundary graphene nanoribbons and their application in switching/demultiplexing. Appl Phys Lett 2013;103:133104.
[61] Mechelen TV, Jacob Z. Universal spin-momentum locking of evanescent waves. Optica 2016;3:118–26.
[62] Aiello A, Banzer P, Neugebauer M, Leuchs G. From transverse angular momentum to photonic wheels. Nat Photon 2015;9:789–95.
[63] Berry MV. Optical currents. J Opt A: Pure Appl Opt 2009;11:094001.
[64] Bliokh KY, Rodríguez-Fortuño FJ, Nori F, Zayats AV. Spin-orbit interactions of light. Nat Photon 2015;9:796–808.
[65] Rodríguez-Fortuño FJ, Marino G, Ginzburg P, et al. Near-field interference for the unidirectional excitation of electromagnetic guided modes. Science 2013;340:328–30.
[66] Lodahl P, Mahmoodian S, Stobbe S, et al. Chiral quantum optics. Nature 2017;541:473–80.
[67] Wang R, Xia H, Zhang D, et al. Bloch surface waves confined in one dimension with a single polymeric nanofiber. Nat Commun 2017;8:14330.
[68] Bakker RM, Yu YF, Paniagua-Domínguez R, Luk'yanchuk B, Kuznetsov AI. Resonant light guiding along a chain of silicon nanoparticles. Nano Lett 2017;17:3458–64.
[69] Bian Y, Ren Q, Kang L, Yue T, Werner PL, Werner DH. Deep-subwavelength light transmission in hybrid nanowire-loaded silicon nano-rib waveguides. Photon Res 2018;6:37–45.
[70] Zhang Y, Xu Y, Tian C, et al. Terahertz spoof surface-plasmon-polariton subwavelength waveguide. Photon Res 2018;6:18–23.
[71] Liang Y, Yu H, Zhang HC, Yang C, Cui TJ. On-chip sub-terahertz surface plasmon polariton transmission lines in CMOS. Sci Rep 2015;5:14853.
[72] Ukhtary MS, Nugraha ART, Hasdeo EH, Saito R. Broadband transverse electric surface wave in silicene. Appl Phys Lett 2016;109:063103.
[73] Musa MY, Renuka M, Lin X, et al. Confined transverse electric phonon polaritons in hexagonal boron nitrides. 2D Mater 2018;5:015018.